Journal of Alloys and Compounds 976 (2024) 172974

Contents lists available at ScienceDirect

Journal of Alloys and Compounds

journal homepage: www.elsevier.com/locate/jalcom

Ironing out the transition metal contribution to the magnetism of the $n = 3$ members of the homologous series $Pr_{n+1}M_nGe_{3n+1}$ (M = Fe, Co): $Pr_4Fe_3Ge_{10}$ vs. $Pr_4Co_3Ge_{10}$

Melissa G. Anderson [a], Trent M. Kyrk [a], Muhammad Zaeem Idrees [b], Sebastian A. Stoian [b], Gregory T. McCandless [a], Ryan E. Baumbach [c], Julia Y. Chan [a,*]

[a] Department of Chemistry and Biochemistry, Baylor University, Waco, TX 76798, United States
[b] Department of Chemistry, University of Idaho, Moscow, ID 83844, United States
[c] National High Magnetic Field Laboratory, Florida State University, Tallahassee, FL 32310, United States

ARTICLE INFO

Keywords:
Rare earth iron germanides
Crystal growth
Disordered systems
Magnetism
Mössbauer spectroscopy

ABSTRACT

The $Ln_{n+1}M_nX_{3n+1}$ (Ln = lanthanide, M = transition metal, and X = tetrel) homologous series provides a platform to study collective phenomena in quantum materials. In this work, we compare the crystal growth, structure, and magnetic properties of the $n = 3$ members of the $Pr_{n+1}M_nGe_{3n+1}$ (M = Fe, Co) analogues, $Pr_4Fe_3Ge_{10}$ ($a = 4.3207$ (10) Å, $b = 35.523$ (8) Å, $c = 4.2982$ (15) Å, and $V = 659.7$ (3) Å^3) and $Pr_4Co_3Ge_{10}$ ($a = 4.3091$ (12) Å, $b = 35.750$ (9) Å, $c = 4.2807$ (11) Å, and $V = 659.4$ (3) Å^3). We determined that the ideal flux growth conditions for each compound are highly dependent on the concentration of Sn flux and quench temperature. $Pr_4Fe_3Ge_{10}$ orders ferromagnetically at 10 K along the *c*-direction while $Pr_4Co_3Ge_{10}$ orders antiferromagnetically at 16 K along the *b*-direction. For both compounds, we observed a magnetic moment higher than that expected for only Pr^{3+} ions (3.58 μ_B/Pr), implying that the transition metal ions contribute to magnetic ordering (3.91, 3.48, and 3.69 μ_B/Pr for $Pr_4Fe_3Ge_{10}$, and 3.76, 4.04, and 3.83 μ_B/Pr for $Pr_4Co_3Ge_{10}$ measured along the *a*-, *b*-, and *c*-directions, respectively). Moreover, the zero-field Mössbauer spectrum obtained at 4.2 K for $Pr_4Fe_3Ge_{10}$ demonstrates that the iron sites participate in magnetic ordering.

1. Introduction

The recently discovered $Ln_{n+1}M_nX_{3n+1}$ (Ln = lanthanide, M = transition metal, and X = tetrel) homologous series [1] is a heterostructure of four subunits, including the $BaNiSn_3$ [2], $CeNiSi_2$ [3], $ThSi_2$ [4], and $AuCu_3$-type structures [5], as shown in Fig. 1. This homologous series provides a platform to investigate the hybridization of *f*-electrons with conduction electrons through systematic substitution of rare earth metals, transition metals, and structural subunits. The magnetic and transport properties of the strongly correlated $Ce_{n+1}Co_nGe_{3n+1}$ analogues were investigated as a function of stacking [1] for $n = 1$ [6], $n = 4$ – 6 [7–10], and $n = \infty$ [11]. $CeCo_{0.89}Ge_2$ ("Ce_2CoGe_4") [12,13], $Ce_6Co_5Ge_{16}$ [9], and $Ce_7Co_6Ge_{19}$ [10] exhibit an elevated electron mass attributed to the Kondo effect with a Sommerfeld coefficient in the range of γ = 123–760 mJ/mol K^2 that increases with additional $BaNiSn_3$ subunits. However, the Sommerfeld coefficient of the $n = \infty$ member, $CeCoGe_3$, is smaller than expected based on this trend (γ = 32 mJ/mol K^2) [11]. The isolated $AuCu_3$ subunit, $CeSn_3$ [14], also does not account for the increase in effective electron mass (γ = 56 mJ/mol K^2), indicating that the strongly correlated nature of this series emerges from the interaction of the subunits. Additionally, the magnetic properties in the $Ce_{n+1}Co_nGe_{3n+1}$ $n = 4$ – 6 analogues exhibit an increase in complexity with increasing n [7], with as many as five distinct transition temperatures observed in $Ce_7Co_6Ge_{19}$ [10]. Based on the trends present across the Ce members of the homologous series, we seek to investigate how new magnetic interactions and quantum phenomena emerge as a function of stacking for other lanthanides, specifically Pr.

The growth of Pr-based intermetallic compounds is motivated by the discovery of weak mixed valency in $PrNi_5$ and $PrFe_{10}Mo_2$ [15], heavy fermion behavior in $PrInAg_2$ [16], Weyl semimetal behavior in PrAlGe [17–19], and unconventional superconductivity in $PrOs_4Sb_{12}$ [20,21]. The $Ln_{n+1}M_nX_{3n+1}$ series has proven to be a robust platform for systematically investigating Pr compounds, including $Pr_3Co_2Ge_7$ [22], $Pr_4Co_3Ge_{10}$ [23], and $Pr_5Co_4Ge_{13}$ [23]. Notably, an elevated effective

* Corresponding author.
E-mail address: Julia_Chan@baylor.edu (J.Y. Chan).

https://doi.org/10.1016/j.jallcom.2023.172974
Received 27 October 2023; Received in revised form 20 November 2023; Accepted 25 November 2023
Available online 30 November 2023

magnetic moment was reported for $Pr_3Co_2Ge_7$ indicating a transition metal magnetic contribution that is absent in Ce analogues of higher *n*. This leads us to investigate the potential for transition metal-lanthanide interactions in Pr members of the homologous series.

Recently, it has been suggested in the $ThCr_2Si_2$ structure type that Fe substitution can be utilized to increase hybridization strength between *f* and conduction electrons [24]. Similarly, the transition metal has been found to have significant impact on the structure and properties of the homologous series. For example, in CeM_xGe_2 (M = Fe, Co, Ni, Cu), the Ni, Co, and Cu analogues are antiferromagnetic Kondo lattices, while the Fe analog exhibits non-magnetic Kondo lattice behavior [25]. Additionally, in $CuFe_2Ge_2$, the substitution of Fe for Co reduces the density of states at the Fermi level and suppresses itinerant magnetic ordering [26]. Within the $BaNiSn_3$ structure type, $CeFeGe_3$ [27] is a concentrated Kondo antiferromagnet, while $CeCoGe_3$ [11] is an RKKY dominated antiferromagnet. Studies on $CeCo_{1-x}Fe_xGe_3$ [28] showed that RKKY and Kondo interactions could be tuned with Fe composition. In this manuscript, we show that antiferromagnetic and ferromagnetic interactions are dependent on the transition metal selection in $Pr_{n+1}M_nGe_{3n+1}$ (M = Fe, Co) through single crystal X-ray diffraction, bulk magnetic measurements, and Mössbauer spectroscopy.

2. Experimental

2.1. Synthesis

As previously reported, $Pr_4Co_3Ge_{10}$ was synthesized using Sn flux [23]. Similarly, single crystals of $Pr_4Fe_3Ge_{10}$ were also grown using Sn flux with a Pr:Fe:Ge:Sn reaction ratio of 3:2:7:30. The elements were placed in an alumina Canfield crucible [29] and flame sealed in a fused silica tube with a pressure of 1/3 atm of Ar gas. The reaction was placed in a furnace and heated to 1175 °C at a rate of 100 °C/h, annealed for 48 h, and cooled to 685 °C at a rate of 2 °C/h. The reaction was then annealed at a final temperature of 685 °C for 48 h. The tube was then removed from the furnace and centrifuged for 5 min to remove the unreacted Sn. The sample was etched with 1:2 HCl:H_2O to remove trace amounts of Sn present on the surface of the crystals. The plate-like morphology of $Pr_4Fe_3Ge_{10}$, as shown in Fig. 2, ranges from 1 to 3 mm in length. The maximum reaction temperature of 1175 °C for $Pr_4Fe_3Ge_{10}$ is the same as the previously reported crystal growth of $Pr_4Co_3Ge_{10}$, which used a different Pr:Co:Ge:Sn reaction ratio of 3:2:7:50 and was cooled to 815 °C [23]. Notably, the optimal synthesis parameters for crystal growth differ with the selection of Fe versus Co in Pr homologous series members.

Reaction parameters, such as starting composition, maximum reaction temperature, ramp rate, and final annealing temperature, were optimized for the growth of $Pr_4Fe_3Ge_{10}$, resulting in yields of 68–88% along with binary compounds such as dendritic crystals of $Fe_{1.6}Ge$ [30] and $PrSn_3$ [31], which were mechanically separated from the sample. We observed that the concentration of Sn flux affects binary formation. For example, when the reaction ratio was changed to 3:2:7:50 and quenched at 815 °C, only $Fe_{1.6}Ge$ was obtained. Other modifications to the reaction parameters, such as decreasing the concentration of Sn from 3:2:7:30–3:2:7:15 and increasing the final annealing temperature to 815 °C, yielded crystals of $Pr_4Fe_3Ge_{10}$ that were 1 mm (or less) in length. A reaction ratio of 1:1:3:20 with a maximum temperature of 1200 °C and a quench temperature of 500 °C also yielded 1 mm crystals of $Pr_4Fe_3Ge_{10}$, indicating its stability over a wide range of final annealing temperatures and starting material concentrations. A 3:2:7:30 reaction ratio and a lower quench temperature of 715 °C yielded larger (2 mm in length) single crystals. Crystal size was further increased (3 mm in length) by maintaining a reaction ratio of 3:2:7:30 but reducing the final annealing temperature to 685 °C, from which samples were used in magnetic measurements. The concentration of Fe ranges from 2.92 (1) – 2.97 (1) while the concentration of Sn ranges from 0.59 (4) – 0.63 (4), based on single crystal X-ray diffraction from batch to batch.

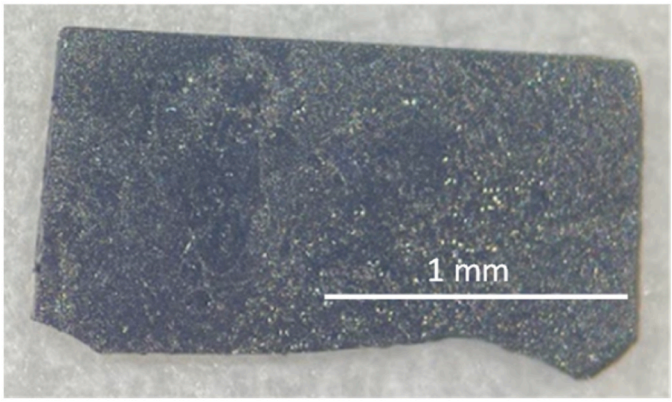

Fig. 2. A representative crystal of $Pr_4Fe_3Ge_{10}$.

2.2. Single crystal X-ray diffraction

Single crystals (with approximate dimensions 0.01 mm x 0.01 mm x 0.02 mm) of $Pr_4Fe_{2.97(1)}Ge_{9.37(4)}Sn_{0.63(4)}$, which will be denoted as $Pr_4Fe_3Ge_{10}$ for simplicity throughout the text, were mounted on glass fibers using two-part epoxy. Data sets for single crystal X-ray diffraction were collected at room temperature on a Bruker D8 Quest Kappa X-ray diffractometer. The diffractometer was equipped with a PHOTON III

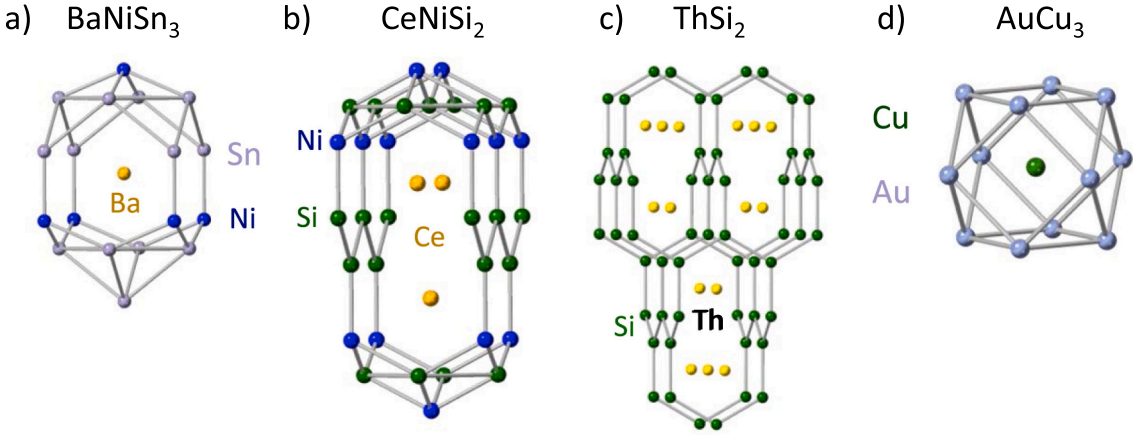

Fig. 1. The crystal structures of the structure types (a) $BaNiSn_3$, (b) $CeNiSi_2$, (c) $ThSi_2$, and (d) $AuCu_3$ are shown to illustrate the relationship between the stacking units of the homologous series $Ln_{n+1}M_nX_{3n+1}$ (Ln = lanthanide, M = transition metal, and X = tetrel).

CPAD detector, HELIOS optics monochromator, and IμS microfocus source (Mo Kα, $\lambda = 0.71073$ Å). Diffraction data was integrated with the Bruker SAINT program while a multiscan method from the SADABS 2016/2 program was used to correct intensities for absorption [32]. SHELXT [33] was employed to generate a preliminary starting model using intrinsic phasing and the model was then anisotropically refined using SHELXL [34].

2.3. Powder X-ray diffraction

Powder X-ray diffraction data was collected on select plate-like crystals that were ground using an agate mortar and pestle. The collection for $Pr_4Fe_3Ge_{10}$ was performed using a Bruker D2 Phaser diffractometer with Cu Kα radiation ($\lambda = 1.54184$ Å). The instrument operated at 30 kV/10 mA with a LYNXEYE XE-T detector. TOPAS was used to perform Rietveld refinement. All reflections are indexed as a single-phase with the occupancies constrained to the single crystal model for $Pr_4Fe_3Ge_{10}$ (see Fig. S1). The lattice parameters obtained from Rietveld refinement are as follows: $a = 4.3309$ (9) Å, $b = 35.6028$ (44) Å, $c = 4.3115$ (9) Å, and $V = 664.8$ (2) Å^3. The powder X-ray diffraction of $Pr_4Co_3Ge_{10}$ was previously reported with lattice parameters of $a = 4.36710$ (14) Å, $b = 35.6931$ (63) Å, $c = 4.20920$ (14) Å, and V = 656.113(34) Å^3 [23].

2.4. Energy-dispersive X-ray spectroscopy

Energy-dispersive spectroscopy (EDS) was carried out using a VERSA 3D focused ion beam scanning electron microscope on single crystals of $Pr_4Fe_3Ge_{10}$ (see Fig. 3) to confirm the incorporation of Sn (see Section 3.1). The formula (normalized to Pr) was determined from the average of four scans at select points on the crystal. The chemical formula obtained from EDS, $Pr_4Fe_{3.07(2)}Ge_{8.47(4)}Sn_{0.68(1)}$, is in agreement with the formula $Pr_4Fe_{2.97(1)}Ge_{9.37(4)}Sn_{0.63(4)}$ from single crystal refinement.

2.5. Laue X-ray diffraction

X-ray backscattering images were obtained using a Photonic Science Laue system AL048 with a Thermo Kevex DXS-11-5025 X-ray source, a tungsten target, and a dual lens coupled Laue camera. The X-ray backscattering images from single crystals of $Pr_4Fe_3Ge_{10}$ were obtained to ensure the absence of any impurity phases on the surface of the crystal as well as provide confirmation of the single crystallinity of the sample (Fig. S2).

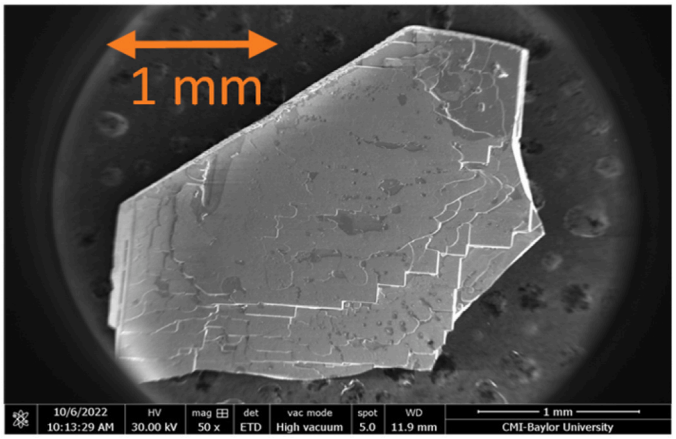

Fig. 3. A representative crystal of $Pr_4Fe_3Ge_{10}$ used for EDS is shown.

2.6. Magnetic property measurements

Magnetic properties were measured using a Quantum Design Magnetic Property Measurement System (MPMS for $Pr_4Fe_3Ge_{10}$ and MPMS3 for $Pr_4Co_3Ge_{10}$). Field dependent measurements were measured for $Pr_4Co_3Ge_{10}$ at 1.8 K from -7 to 7 T. Additionally, data was collected at 1.8 K, 5 K, 10 K, and 15 K from -7 to 7 T for $Pr_4Fe_3Ge_{10}$. Temperature dependent magnetic susceptibility was measured with an applied field of 0.1 T along all three crystallographic directions of the crystals under zero-field cooled (ZFC) and field cooled (FC) conditions.

2.7. ^{57}Fe Mössbauer spectra

Nuclear Gamma Resonance (Mössbauer) spectra were recorded using a spectrometer operated in a constant acceleration mode. This instrument was equipped with a Janis 8DT Varitemp cryostat which incorporated a superconducting coil cooled with liquid helium. The spectra obtained at room temperature (RT) were recorded while the cryostat was warmed at RT. Isomer shifts are reported with respect to the center of a zero-field spectrum recorded for a metal foil of α-iron. The absorbers used in this study have been prepared by dispersing ground crystalline powders in eicosane which functioned as an inert support. The data was analyzed using the WMOSS (See Co formerly Web Research Co, Edina MN) and C-based Igor Pro codes written in house. The RT spectrum was simulated considering either one or two quadrupole doublets. In contrast, the 4.2 K spectrum was analyzed using the model developed by Rancourt and Ping [35,36] which allowed us to determine the effective fields acting on the iron nuclei by considering an arbitrary distribution of hyperfine fields.

3. Results and discussion

3.1. $Pr_4Fe_3Ge_{10}$ structure

The $n = 3$ members of the $Pr_{n+1}M_nGe_{3n+1}$ (M = Fe, Co) homologous series are isostructural to $Eu_2Ni_{2-x}Sn_5$ ("$Eu_4Ni_3Sn_{10}$") [37] and contain $CeNiSi_2$ [3], $ThSi_2$ [4], $AuCu_3$ [5], and $BaNiSn_3$ [2] -type subunits, as shown in Fig. 4. The flux-growth and structure of the Co analog $Pr_4Co_3Ge_{10}$ was previously reported in the space group *Cmcm* with lattice parameters of $a = 4.3091$ (12) Å, $b = 35.750$ (9) Å, $c = 4.2807$ (11) Å, and $V = 659.4$ (3) Å^3 [23]. $Pr_4Fe_3Ge_{10}$ also crystallizes in the orthorhombic *Cmcm* space group with lattice parameters of $a = 4.3207$ (10) Å, $b = 35.523$ (8) Å, $c = 4.2982$ (15) Å, and $V = 659.7$ (3) Å^3 as summarized in Table 1. The structure consists of two Pr, two Fe, and six tetrel sites with the special position 4*c* (*m*2*m*) (Table S1). The Pr2 local environment can be represented by either the $ThSi_2$ or $CeNiSi_2$ structure types (Fig. 4b), containing ten germanium atoms and four iron atoms. Pr2 is in contact with 6 other Pr2 atoms with distances of 3.9949 (10) Å x 2, 4.2982 (15) Å x 2 and 4.3207 (10) Å x 2 (Table 2).

The Pr1 local environment is a disordered polyhedron related to the $BaNiSn_3$ and $AuCu_3$ structure types; comprised of twelve germanium, six iron, and four tin atoms. Pr1 is in contact with four other Pr1 atoms with distances of 4.2982 (15) Å x 2 and 4.3207 (10) Å x 2 (Table 2). Without the consideration of the $AuCu_3$ subunit represented by the Sn5B site in the anisotropic model, a residual electron density of 7.98 e$^-$ Å^{-3} and a hole of -9.59 e$^-$ Å^{-3} were observed less than 1 Å from a prolated Ge5A site. As a result, the Sn5B site (Fig. 4c) was added to the model based on the interatomic distances of neighboring Ge2 atoms (3.2767 (29) Å x2) and the suggestion of Sn incorporation from EDS. This change was successful in reducing the prolation of the Ge5A site. With the Fe1A and Ge5A occupancies constrained to be equal and the sum of the Ge5A and Sn5B sites constrained to be 100%, elevated residual electron densities of 4.74 e$^-$ Å^{-3} (0.11 Å from Ge5A) and -10.12 e$^-$ Å^{-3} (0.27 Å from Fe1A) were observed. Therefore, the Fe1A site occupancy was allowed to refine freely from the Ge5A site, as done with previously published $n = 3$ analogues [22,37]. After considering partial Fe1A occupancies, the

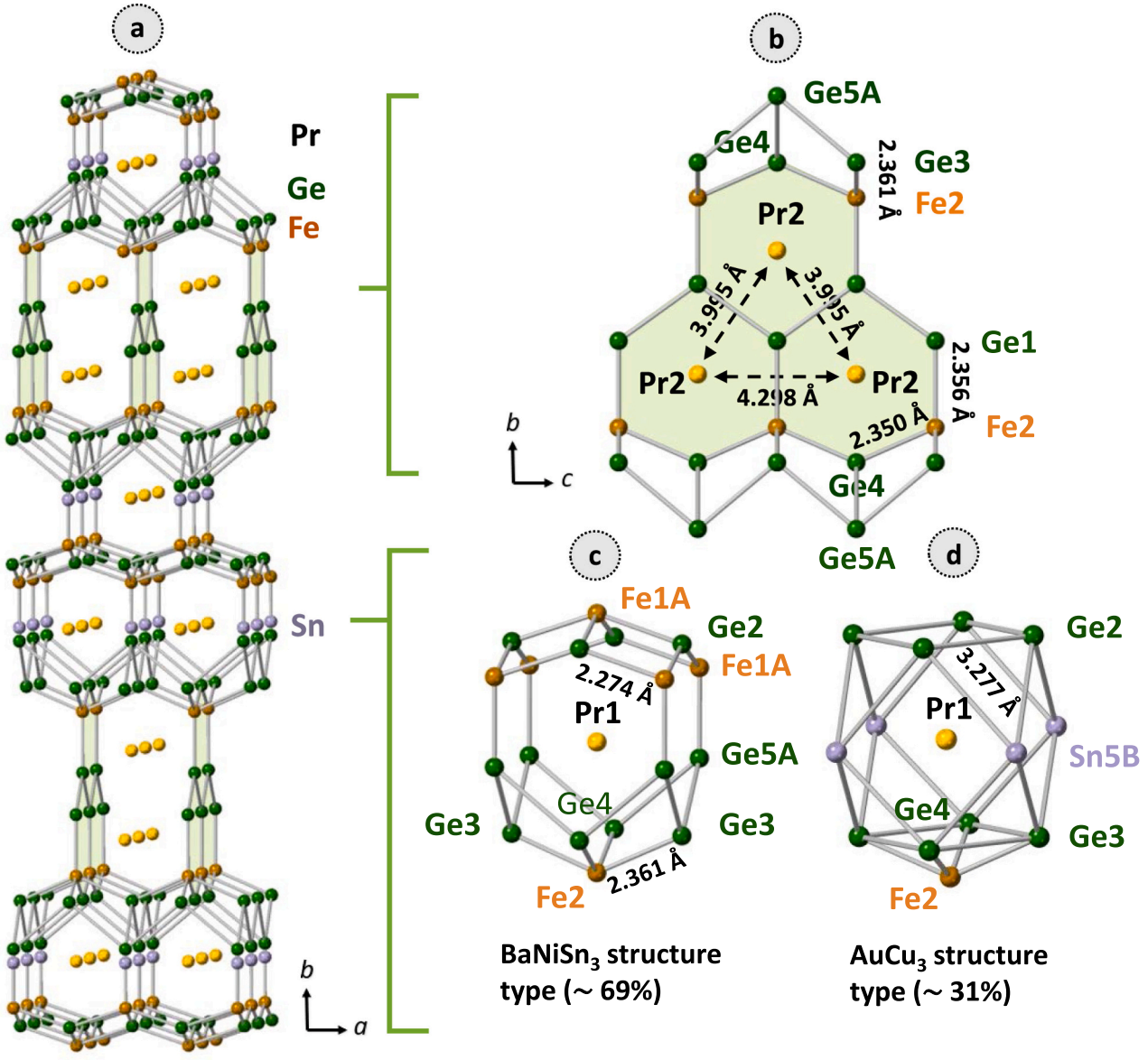

Fig. 4. The atoms, Pr, Fe, Ge, and Sn are shown as yellow, dark orange, green, and purple, respectively. The structure of $Pr_4Fe_3Ge_{10}$ is viewed along the *c*-axis (a). The $CeNiSi_2$ subunit contains Pr2 atomic sites as shown in (b) with the $ThSi_2$ structure type highlighted in green. The disorder model for $Pr_4Fe_3Ge_{10}$ is shown for the Pr1 local environment and can be broken down into two partially occupied structure types: $BaNiSn_3$ (c) and $AuCu_3$ (d), with the percent occupancy specified.

residual electron densities further reduced to 2.6 e^- $Å^{-3}$ and -4.9 e^- $Å^{-3}$. Additionally, the Fe2 site occupancy was allowed to refine, but remained near unity and was constrained to full occupancy. In summary, two configurations are present in the disordered model of the Pr1 local environment: the Fe1A – Ge5A dimer, representing the occupancy of the $BaNiSn_3$ subunit (~ 69%) (Fig. 4c) with Fe vacancies, and the Sn5B site, representing the occupancy of the $AuCu_3$ subunit (~ 31%) (Fig. 4d).

As summarized in Table 2, the Ge–Ge bond distances in $Pr_4Fe_3Ge_{10}$ are 2.6474 (14) Å (Ge1–Ge1) in the $CeNiSi_2$ subunit and 2.8111 (19) Å (Ge4–Ge5A) in the $BaNiSn_3$ subunit, which agree with the bond lengths present in $PrFeGe_2$ (2.629 Å) and $PrFeGe_3$ (2.776 Å) [38,39]. The Fe–Ge bond distances (2.259 (5) Å - 2.3613 (9) Å) are comparable to $PrFeGe_3$ and $PrFeGe_2$ (2.269–2.395 Å) [38,39]. Additionally, Pr-Ge bond distances (3.0916 (8) Å – 3.1680 (11) Å) are in agreement with previously reported interatomic distances found in $PrGe_{3.36}$ [40] and Pr_4Ge_7 [41] (see Table S2).

The composition of the parent structure, $Eu_2Ni_{2-x}Sn_5$, depends on the synthesis method: $Eu_2Ni_{1.49(1)}Sn_5$ was grown from a self-flux and $Eu_2Ni_{1.35(1)}Sn_5$ was arc-melted [37]. $Eu_2Ni_{2-x}Sn_5$ (x = 0.65 and 0.51), contains Sn5A and Sn5B sites which are analogous to the Ge5A and Sn5B sites in the model for $Pr_4Fe_3Ge_{10}$ (see Table 1 and Figs. 4c and 4d) [37]. When comparing the flux-grown $Eu_2Ni_{1.49}Sn_5$ and $Pr_4Fe_3Ge_{10}$, the M1 (M = Fe, Ni) site occupancies are equal at ~ 48%; however, the occupancies of the disordered tetrel sites differ from ~ 53% and ~ 47% for Sn5A and Sn5B in $Eu_2Ni_{1.49}Sn_5$ to ~ 69% and ~ 31% for Ge5A and Sn5B in $Pr_4Fe_3Ge_{10}$. In $Pr_4Co_3Ge_{10}$, an additional orientation of the $BaNiSn_3$ subunit is present in the disordered Pr1 local environment with the Co1A–Ge5A dimer ~ 67% occupied, the Co1B–Ge5B dimer ~ 8% occupied, and the Sn1 site ~ 25% occupied [23]. The Co sites within the Co–Ge dimers are also partially occupied with Co1A ~ 58% occupied and Co1B ~ 5% occupied.

3.2. *Magnetic properties*

3.2.1. *$Pr_4Fe_3Ge_{10}$*

The temperature dependent magnetic susceptibility of $Pr_4Fe_3Ge_{10}$ (Fig. 5) was measured along the *a*-, *b*-, and *c*-directions, the results of which are summarized in Table 3, where θ_{CW}

Table 1
Crystallographic data, data collection, and refinement parameters.

Empirical formula	$Pr_4Fe_{2.97\ (1)}Ge_{9.37\ (4)}Sn_{0.63\ (4)}$
Space group	*Cmcm* (no. 63)
Lattice parameters	
a (Å)	4.3207(10)
b (Å)	35.523(8)
c (Å)	4.2982(15)
Volume [Å^3]	659.7(3)
Z	2
Density [g/cm^3]	7.472
Absorption coefficient [mm^{-1}]	39.70
F(000)	1289
Crystal size [mm^3]	0.01 × 0.01 × 0.02
θ range [°]	2.3–30.5
Index range	
h	-6 → 6
k	-50 → 50
l	-6 → 6
Number of reflections	11,813
Unique reflections	637
Parameters/restraints	39/1
R_{int}	0.065
$\Delta\rho_{max/min}$ (e$^-$ Å^{-3})	2.63/− 4.93
GoF	1.14
$R\ [F^2 > 2\sigma(F^2)]$	0.032
$wR_2\ (F^2)$	0.083

$R = \sum||F_o| - |F_c||/\sum|F_o|$ and $wR_2 = \left\{\sum w\left[(F_o)^2 - (F_c)^2\right]^2 / \sum w\left[(F_o)^2\right]^2\right\}^{1/2}$

Table 2
Select interatomic distances (Å) in $Pr_4M_3Ge_{10}$ (M = Fe, Co).

	$Pr_4Fe_3Ge_{10}$	$Pr_4Co_3Ge_{10}$ [23]
$BaNiSn_3$ subunit		
Pr1-Pr1 (x2)	4.2982 (15)	4.3091 (12)
Pr1-Pr1 (x2)	4.3207 (10)	4.2807 (11)
M1A-M1A (x4)	3.392 (3)	3.566 (3)
Co1B-Co2 (x4)	-	3.554 (15)
M1A-Ge2 (x2)	2.2862 (14)	2.3336 (17)
M1A-Ge5A (x1)	2.259 (4)	2.248 (5)
Co1B-Ge5B (x1)	-	2.231 (36)
Ge3-Ge5A (x2)	2.8004 (19)	2.715 (2)
Ge4-Ge5A (x2)	2.8111 (19)	2.729 (2)
Ge2-Sn5B (x2)	3.2767 (29)	3.2862 (45)
$CeNiSi_2$ subunit		
Pr2-Pr2 (x2)	3.9949 (10)	4.0011 (9)
Pr2-Pr2 (x2)	4.2982 (15)	4.2807 (11)
Pr2-Pr2 (x2)	4.3207 (10)	4.3091 (12)
M2-M2 (x4)	4.2982 (15)	4.2807 (12)
M2-Ge1 (x1)	2.3558 (19)	2.351 (2)
M2-Ge3 (x2)	2.3613 (9)	2.3652 (11)
M2-Ge4 (x2)	2.3496 (10)	2.3509 (11)
Ge1-Ge1 (x2)	2.6474 (14)	2.6222 (17)

is the Weiss constant, T_N is the Néel temperature, and μ_{eff} is the effective magnetic moment. Fitting the inverse susceptibility (Fig. S3) above 50 K yielded θ_{CW} = -30.0 K and -31.3 K along the *a*- and *b*-directions, respectively (Table 3), indicating antiferromagnetic interactions. However, along the *c*-direction, a positive Weiss constant of 22.0 K is observed, which indicates ferromagnetic interactions. Along the *a*- and *b*-directions, bifurcation of the ZFC and FC is observed in the magnetic susceptibility (Fig. 5, inset). $Pr_4Fe_3Ge_{10}$ exhibits an effective magnetic moment of 3.91, 3.48, and 3.69 μ_B/Pr for the *a*-, *b*-, and *c*-directions, respectively. These values along *a*- and *c*-directions are higher than anticipated for the spin-only magnetic moment of Pr^{3+} (3.58 μ_B) and suggests that Fe contributes to the magnetism.

Fig. 6 shows the field dependent magnetization along all three crystallographic directions at T = 1.8 K, 5 K, 10 K, and 15 K. The magnetization in the *c*-direction is strongly anisotropic, in contrast to

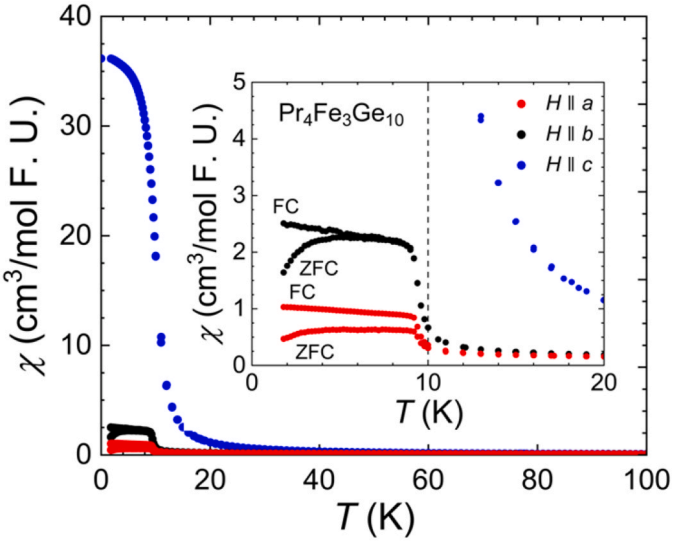

Fig. 5. The magnetic susceptibility (measured at 0.1 T) as a function of temperature is shown for $Pr_4Fe_3Ge_{10}$. Along the *a* (red circles), *b* (black circles), and *c* (blue circles) crystallographic direction. The inset contains a zoomed region to highlight the transition temperature at 10 K and the bifurcation along the *a*- and *b*-direction.

Table 3
Magnetic properties of $Pr_4Fe_3Ge_{10}$ compared to $Pr_4Co_3Ge_{10}$ at H = 0.1 T.

	Applied field direction	μ_{eff} (μ_B/Pr)	θ_{CW} (K)	T_N (K)
$Pr_4Fe_3Ge_{10}$	*H // a*	3.91	−30.0	10
	H // b	3.48	−31.3	10
	H // c	3.69	22.0	10
$Pr_4Co_3Ge_{10}$	*H // a*	3.76	−31.6	-
	H // b	4.04	−42.6	16
	H // c	3.83	−34.1	-

the magnetization in the *a*- and *b*-directions. There is a slight hysteresis present (Fig. S4) with a small asymmetric kink in the hysteresis for the *a*- and *b*-directions. At 7 T and 1.8 K, the saturation magnetic moment is μ_{sat} = 2.89 μ_B/mol F.U. (formula unit) along the *a*-direction, μ_{sat} = 3.74 μ_B/mol F.U. along the *b*-direction, and μ_{sat} = 8.4 μ_B/mol F.U. along the *c*-direction.

The magnetic properties of the $BaNiSn_3$ and $AuCu_3$ subunits may be compared to the magnetic properties of $Pr_4Fe_3Ge_{10}$. $PrFeGe_3$, ($BaNiSn_3$ structure type) shows similar magnetic properties to $Pr_4Fe_3Ge_{10}$ along the *a*- and *b*- directions with a Weiss constant of - 1.6 K that suggests weak antiferromagnetic interactions, similar to the negative Weiss constants for *H // a* and *H // b*, as well as a lower than expected effective moment of 3.47 μ_B/Pr, similar to *H // b* (3.48 μ_B/Pr) [42]. However, $Pr_4Fe_3Ge_{10}$ only has a negative Weiss constant along the *a*- and *b*-directions. The only similarity observed for $PrSn_3$ ($AuCu_3$ structure type) is antiferromagnetic order along the < 100 > and < 110 > directions (T_N = 8.2 K); while unlike $Pr_4Fe_3Ge_{10}$, a lower effective magnetic moment than expected is observed [43]. The Pr2 local environment may be analyzed in terms of the $ThSi_2$ and $CeNiSi_2$ structure types. The polycrystalline $PrGe_{2-x}$ compound ($ThSi_2$ structure type) exhibits a slight hysteresis curve from - 0.10 to 0.10 T at 2 K, a lower than expected effective magnetic moment, and a ferromagnetic ordering temperature at 14.6 K [44]. In contrast, the slight hysteresis seen for $Pr_4Fe_3Ge_{10}$, is present from -0.7 to 0.7 T for the *a*-direction, - 0.5 to 0.5 T for the *b*-direction, and - 0.05 to 0.05 T for the *c*-direction. The structure of $PrFe_{1-x}Ge_2$ (x = 0.32) [38] ($CeNiSi_2$ structure type) has been reported; however, its magnetism is yet to be described. Overall, the magnetic behavior observed for the subunits in this phase space are not identical to the properties present in the stacked heterostructure. Therefore, the

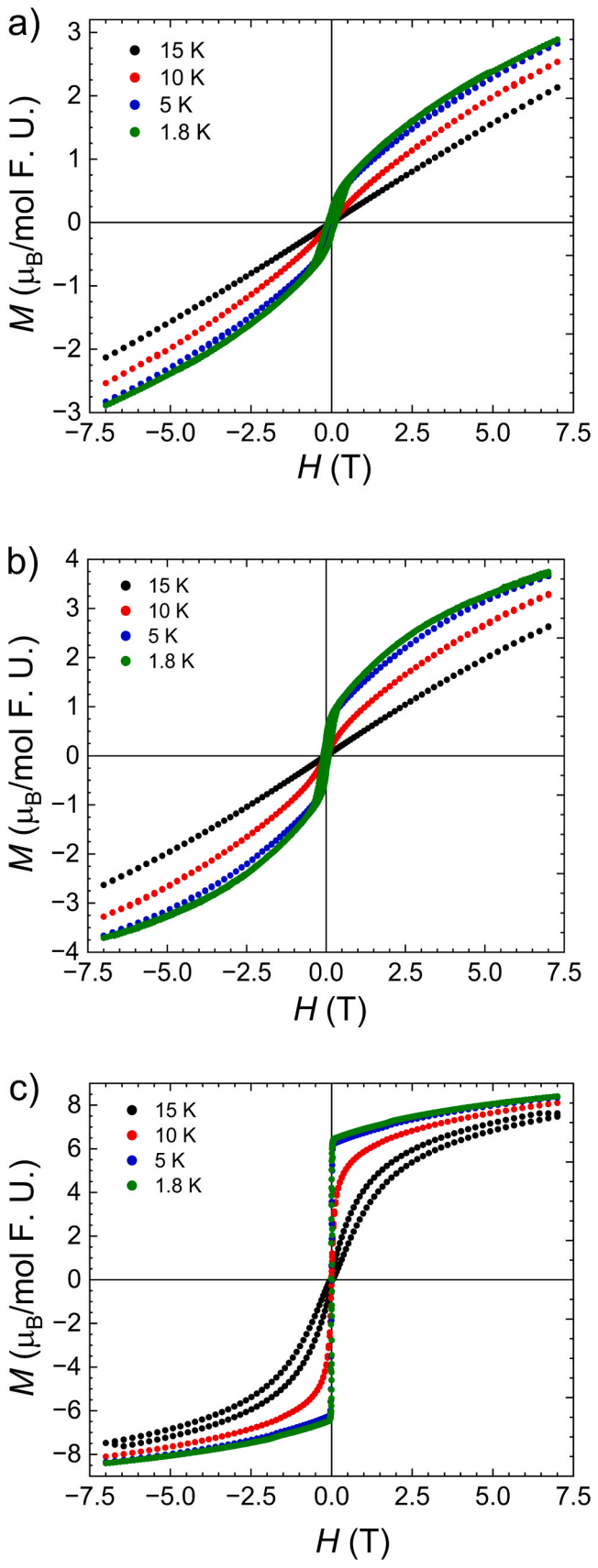

Fig. 6. Magnetization as a function of magnetic field is shown for $Pr_4Fe_3Ge_{10}$ (a) along the *a*-direction ($H||a$), (b) ($H||b$), and (c) ($H||c$). Temperature is held constant at 1.8 K (green circles), 5 K (blue circles), 10 K (red circles), and 15 K (black circles).

stacking interactions of the subunits or separation of subunits is important to the tuning of properties for a desired application.

3.2.2. $Pr_4Co_3Ge_{10}$

As shown in Fig. 7a, the magnetic susceptibility of $Pr_4Co_3Ge_{10}$ exhibits a bifurcation between the ZFC and FC measurements at $T \sim 7$ K with field applied perpendicular to the *c*-direction. In the ZFC, two features are visible at $T_1 = 6.7$ K and $T_2 = 2.9$ K. These features are likely not magnetic transitions as they are only present in the ZFC and not in the FC magnetic susceptibility. The *a*- and *b*-directions exhibit similar behavior, but there is no bifurcation of the ZFC and FC. The bifurcation is reminiscent of the polycrystalline magnetic susceptibility in $Eu_2Ni_{1.50}Sn_5$ below approximately $T = 5$ K [37]. Susceptibility measurements parallel to the *b*-direction reveal an antiferromagnetic transition at $T = 16$ K, but another spin reorientation may appear below 1.8 K. The inverse magnetic susceptibility (Fig. S5) shows Curie-Weiss behavior with θ_{CW} = -31.6 K and $\mu_{eff} = 3.76\ \mu_B$/Pr, θ_{CW} = - 42.6 K and $\mu_{eff} = 4.04\ \mu_B$/Pr, and θ_{CW} = -34.1 K and $\mu_{eff} = 3.83\ \mu_B$/Pr along the *a*-, *b*-, and *c*-directions, respectively. The negative Weiss constants indicate dominantly antiferromagnetic interactions along all three directions, with elevated effective magnetic moments ($\mu_{calc} = 3.58\ \mu_B/Pr^{3+}$) suggesting magnetic contribution from the Co sublattice. Notably, the Co contribution to the magnetic moment is not observed in the Ce analogues of this homologous series [7,9,10], but is observed in $Pr_3Co_2Ge_7$ suggesting that the 3*d*-4*f* interactions are markedly different for Pr [22].

Fig. 7b shows the field dependent magnetization measured at 1.8 K. Up to applied fields of 7 T, the magnetization does not approach the expected magnetic saturation for Pr^{3+} of $\mu_{sat} = 12.8\ \mu_B$/F.U. instead reaching significantly lower values $\mu_{sat} = 2.28\ \mu_B$/F.U., 3.16 μ_B/F.U., and 2.36 μ_B/F.U., along the *a*-, *b*-, and *c*-directions, respectively. These properties are similar to the partially Sn substituted analog of $Pr_3Co_2Ge_7$ which attains a magnetization of $\mu_{sat} \approx 1.95\ \mu_B$/F.U. We note that, unlike $Pr_3Co_2Ge_7$, $Pr_4Co_3Ge_{10}$ exhibits no evidence of metamagnetic transitions below 7 T. The reduced saturation magnetic moment resembles the behavior of polycrystalline $Eu_2Ni_{1.50}Sn_5$ which also had a saturation moment nearly half that expected for Eu^{2+} [37]. As reflected in the magnetic susceptibility measurements, the magnetization of $Pr_4Co_3Ge_{10}$ along the *a*- and *c*-directions are most similar, with a weak curvature and small hysteresis up to an applied field of $H = 0.5$ T like that observed in $PrGe_{2-x}$ [44] and $Pr_4Fe_3Ge_{10}$ (Fig. S6). This is contrasted by the uniform hysteresis present up to $H = 7.0$ T along the *b*-direction. It should be noted that $Pr_2Co_3Ge_5$ is often present as a coproduct with $Pr_4Co_3Ge_{10}$, as is discussed elsewhere [23]. The powder diffraction pattern obtained for the measured $Pr_4Co_3Ge_{10}$ sample shows no presence of $Pr_2Co_3Ge_5$ and the magnetic behavior of $Pr_4Co_3Ge_{10}$ is distinctly different. Both polymorphs of $Pr_2Co_3Ge_5$ show broad magnetic ordering at T = 30-36 K and T = 5 - 10 K with no bifurcation of the ZFC and FC measurements [45,46]. The effective magnetic moments obtained for $Pr_2Co_3Ge_5$ when normalized to Pr also show elevated values in a range of μ_{eff} = 3.77 - 4.07 μ_B/Pr depending on the measured direction, similar to what is observed for $Pr_4Co_3Ge_{10}$.

Like the $Ce_{n+1}Co_nGe_{3n+1}$ family of compounds [7], the magnetic behavior of $Pr_4Co_3Ge_{10}$ contrasts that of its structural building blocks. As previously mentioned, $PrCoGe_3$ ($BaNiSn_3$ structure type) was reported to be paramagnetic down to 1.8 K with no indication of Co contribution to the paramagnetic effective moment [47]. Interestingly, the magnetic properties of $PrCoGe_3$ are more anisotropic than $Pr_4Co_3Ge_{10}$ where the magnetic response with field applied along the long axis of the unit cell is nearly ten times greater than along the *ab*-plane [47]. In contrast, $Pr_4Co_3Ge_{10}$ behaves significantly less anisotropic, albeit with a characteristic hysteresis present along the long axis that is absent in the *ac*-plane. $PrCo_{0.85}Ge_2$ ($CeNiSi_2$ structure type) adopts a collinear antiferromagnetic order with Pr moments aligned anti-parallel to the *c*-axis at 5 K, corresponding approximately to the ordering temperature observed in the ZFC magnetic susceptibility along the *c*-direction of $Pr_4Co_3Ge_{10}$ [48]. However, the saturation magnetic

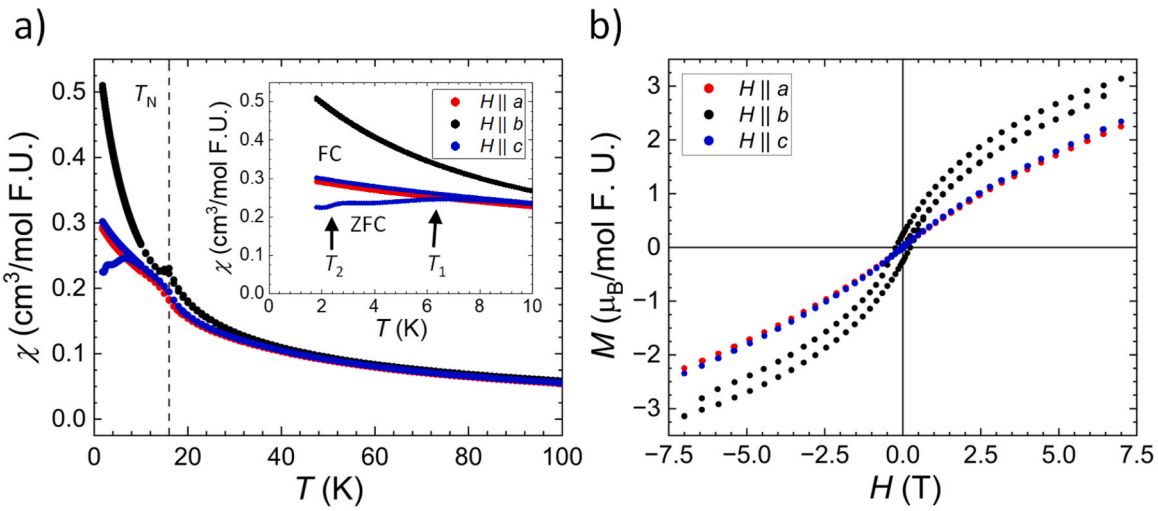

Fig. 7. (a) The magnetic susceptibility (at 0.1 T) as a function of temperature is shown for $Pr_4Co_3Ge_{10}$. (b) Magnetization as a function of magnetic field at 1.8 K is shown for $Pr_4Co_3Ge_{10}$. *H//a*, *H//b*, and *H//c* are shown as red, black, and blue, respectively.

moment (μ_{sat} = 1.5 μ_B/Pr), while still far reduced from the expected magnetic saturation of Pr, is double that of $Pr_4Co_3Ge_{10}$ [48]. The effective magnetic moments of both $PrCoGe_3$ (3.60 μ_B/Pr parallel to *a*- and 3.50 μ_B/Pr parallel to *c*-directions) and $PrCo_{0.85}Ge_2$ (3.63 μ_B/Pr) suggests that there is little to no Co contribution to the magnetism. The reported Weiss constants for $PrCoGe_3$ (θ_{CW} = 6.6 K parallel to *a*- and θ_{CW} = -18 K parallel to *c*-crystallographic directions) and $PrCo_{0.85}Ge_2$ (θ_{CW} = -15 K, polycrystalline) are about half the magnitude of that observed in $Pr_4Co_3Ge_{10}$ [47,48]. Thus, the magnetic properties in this intergrowth structure are a coherent interaction of the subunits distinctly different than the sum of its building blocks, further suggesting that the sequence of the stacking subunits plays a significant role in the properties of the homologous series members.

3.3. Mössbauer spectroscopy

The zero-field RT spectrum obtained for a neat powder sample of $Pr_4Fe_3Ge_{10}$ exhibits an asymmetric doublet (Fig. 8). This spectrum may be fit considering a quadrupole doublet characterized by an isomer shift δ = 0.38 mm/s, quadrupole splitting ΔE_Q = 0.38 mm/s and dissimilar linewidths $\Gamma_{L/R}$ = 0.29/0.35 mm/s, (Fig. S7 and Table 4). However, the presence of two crystallographically distinct iron sites suggests that the observed spectrum originates from the contribution of two distinct spectral components. Therefore, the theoretical RT spectrum was obtained by considering two symmetric quadrupole doublets with a 1:2 relative ratio as inferred from the Fe1A:Fe2 site occupancies. While the dominant spectral component of Fe2 is characterized by parameters which are similar to those obtained considering a single site, the parameters of the minor Fe1A component derived when using two sites are quite different, with the ΔE_Q of Fe1A being 50% larger than that of Fe2 (see Table 4). A larger quadrupole splitting is often indicative of a lower iron site symmetry. However, in this case, the two iron sites occupy the same Wyckoff positions and thus the same site symmetry. Therefore, it is likely that the dissimilar ΔE_Q values of Fe2 and Fe1A are traced to differences in the populations (or site occupancy) of iron's 3*d* orbitals in the average structure. Additionally, the larger isomer shift of the minor component suggests that the Fe1A sites have a lower electron density at the ^{57}Fe nucleus [49]. Inspection of the spectrum recorded at 4.2 K (bottom of Fig. 8) for $Pr_4Fe_3Ge_{10}$ reveals that at this temperature the observed resonances are much broader than at RT (top of Fig. 8). This behavior suggests that this spectrum exhibits an unresolved magnetic hyperfine splitting which likely originates from the onset of magnetic ordering. Using the isomer shift values and the 1:2 relative ratio inferred from single crystal X-ray diffraction data, we estimated that while the

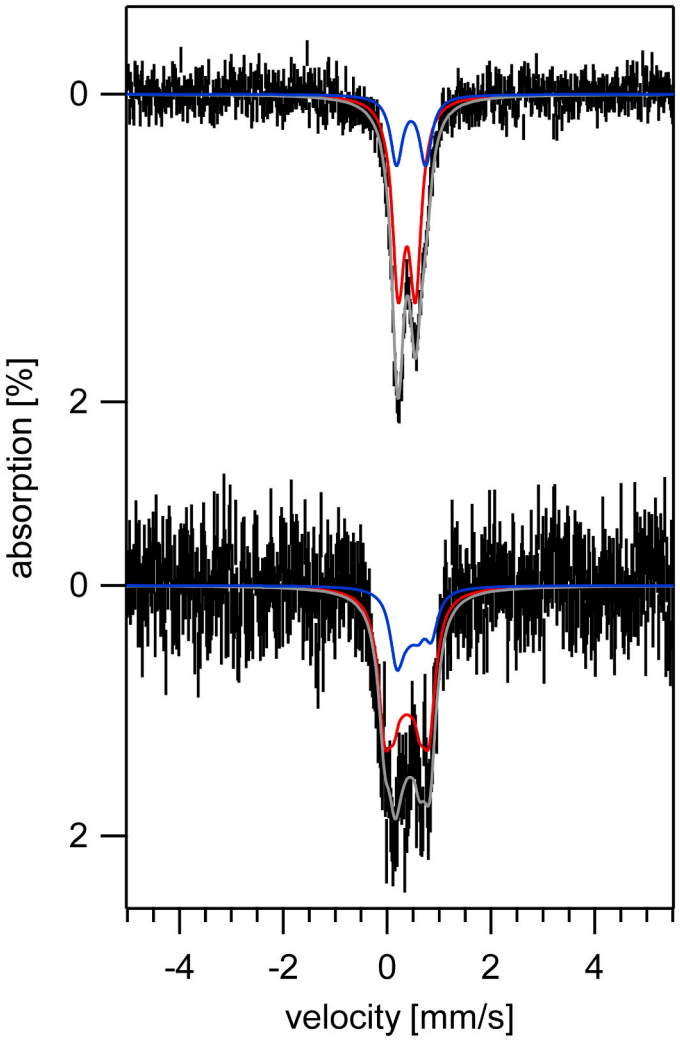

Fig. 8. Zero-field ^{57}Fe Mössbauer spectra recorded at RT (*top*) and 4.2 K (*bottom*) for $Pr_4Fe_3Ge_{10}$. The theoretical spectra were obtained using the parameters listed in Table 3.

Table 4
Zero-field ^{57}Fe Mössbauer parameters derived from the analysis of the RT spectrum recorded for $Pr_4Fe_3Ge_{10}$.

Model	Site	δ [mm/s]	ΔE_Q [mm/s]	$\Gamma_{L/R}$ [mm/s]	B_{int}[a] [T]	Area [%]
1 site	Red	0.38	0.38	0.29/0.35	n.a.	100
2 sites	Red (Fe2)	0.37	0.32	0.28	2.65	66
	Blue (Fe1A)	0.45	0.48	0.28	2.06	33

[a] Internal magnetic field used to simulate the spectrum recorded at 4.2 K. In this case the electric field gradient tensor component along the internal field was set to zero.

spontaneous magnetic field acting on the Fe2 sites is $B_{int} \sim 2.65$ T, that acting on the Fe1A sites associated with the minor component is somewhat smaller $B_{int} \sim 2.06$ T. For these simulations we have set the electric field gradient tensor component (ε) along the internal field to zero.

3.4. Discussion

$Pr_4Fe_3Ge_{10}$ and $Pr_4Co_3Ge_{10}$ both show transition metal contributions to the magnetic properties of 2.00 μ_B/mol Fe and 2.17 μ_B/mol Co, respectively. Additionally, both materials exhibit magnetic anisotropy likely stemming from their highly anisotropic crystal structures; however, their magnetism differs significantly. $Pr_4Fe_3Ge_{10}$ exhibits strong magnetic ordering along the *c*-direction compared to the *a*- and *b*-directions, whereas the magnetic ordering in $Pr_4Co_3Ge_{10}$ is significantly weaker, with the *b*-direction differing from the *a*- and *c*-directions. The Curie-Weiss constants of $Pr_4Fe_3Ge_{10}$ indicate that the *a*- and *b*-directions are both antiferromagnetic while the *c*-direction is dominantly ferromagnetic, unlike the Co analog which is antiferromagnetic along all directions (Table 3). Notably, the Pr-Pr interatomic distances of $Pr_4Fe_3Ge_{10}$ and $Pr_4Co_3Ge_{10}$ (Table 2) are similar (less than 0.05 Å difference between equivalent distances), suggesting that Pr alone is not responsible for the differences observed in the magnetism. The behavior of the Fe and Co analogues may be linked to three trends in the disordered subunit of the homologous series: (1) the transition metal occupancy of the $BaNiSn_3$ subunit, (2) the number of orientations of the $BaNiSn_3$ subunit within each disordered Pr1 local environment, and (3) the local environment of the transition metal.

In the germanium analogues of the $CeNiSi_2$ structure type, an increase in transition metal occupancy occurs with increasing transition metal group number [38]. Our results agree with this trend: the concentration of transition metal increases from $Pr_4Fe_{2.97(1)}Ge_{9.37(4)}Sn_{0.63(4)}$ to $Pr_4Co_{3.25(3)}Ge_{9.50(1)}Sn_{0.469(4)}$ [23]. However, the transition metal vacancy does not occur in the $CeNiSi_2$ subunit but in the M-Ge dimer of the $BaNiSn_3$ subunit. The difference in transition metal vacancies for $Pr_4Fe_3Ge_{10}$ (~ 21%) compared to $Pr_4Co_3Ge_{10}$ (~ 12% summed between the Co1A and Co1B sites) may affect the transition metal contribution to the magnetic properties. Vacancy dependent magnetism has been reported in compounds isostructural to $CeNiSi_2$. For example, decreasing Ni occupancy in $TbNi_xGe_2$ results in a decrease of the Néel temperature where concentrations of $x = 1$, 0.6, and 0.4 result in transition temperatures of 37 K, 31 K, and 16 K, respectively [50–52]. Additionally, in CeM_xGe_2 (M = Fe, Co, Ni, Cu; $x = 1 - 0.53$), the transition metal occupancy was correlated with changes in broad features of the electrical

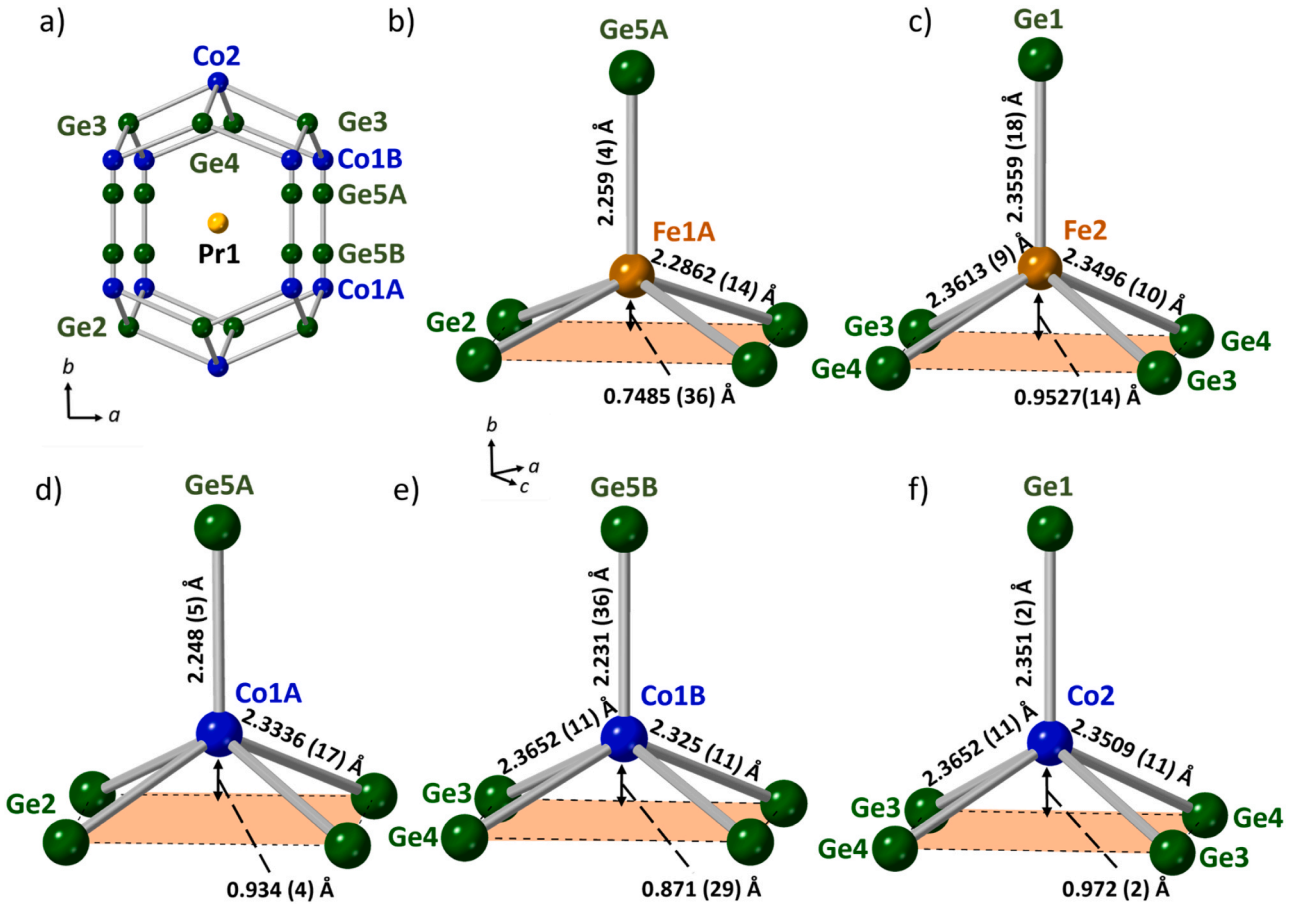

Fig. 9. (a) The disorder of the $BaNiSn_3$ subunit in $Pr_4Co_3Ge_{10}$ is shown with the typical orientation marked as Co1A-Ge5A and the inverted orientation as Co1B-Ge5B. The (b) Fe1A, (c) Fe2, (d) Co1A, (e) Co1B, and (f) Co2 sites are compared for $Pr_4Fe_3Ge_{10}$ and $Pr_4Co_3Ge_{10}$. The transition metal-Ge distances and distance from the basal Ge plane (highlighted in orange) are given.

resistivity linked to Kondo-lattice behavior [25].

$Pr_4Fe_3Ge_{10}$ and $Pr_4Co_3Ge_{10}$ are similar structurally, but differ in their disorder. The disordered subunit of $Pr_4Fe_3Ge_{10}$ consists of either the $AuCu_3$ building block or one orientation of the $BaNiSn_3$ building block, whereas in $Pr_4Co_3Ge_{10}$, the $BaNiSn_3$ block can exist in two orientations [23]. The second $BaNiSn_3$ configuration in $Pr_4Co_3Ge_{10}$ is inverted from the one found in $Pr_4Fe_3Ge_{10}$ and is present only 5% (Fig. 9a). Still, the additional disorder may impact the differences in properties observed between the two analogues. Also, the Fe1A site present in the $BaNiSn_3$ subunits is different compared to the Fe2 site or the Co1A and Co2 sites. As shown in Figs. 9b and 9c, the Fe1A-Ge2 bond distance (2.2735 (15) Å) is significantly contracted compared to the Fe2-Ge3/4 bond distances (2.3496 (10) - 2.3613 (9) Å, Fig. 9c) and Fe2-Ge1 bond distance (2.3558 (19) Å) indicating stronger Fe1A-Ge bonding interactions compared to Fe2-Ge. The Mössbauer spectroscopy also indicates electronic differences between the two Fe sites based on the enhanced quadrupole splitting of the Fe1A site compared to the Fe2 site, despite their equivalent site symmetry (*m*2*m*). In contrast, the Co-Ge bonds in $Pr_4Co_3Ge_{10}$ are more similar. Here, the Co1A-Ge5A and Co1B-Ge5B distances are contracted relative to the Co2-Ge1 distance whereas the Co1A/Co1B-Ge2 distances are similar to the Co2-Ge3/Ge4 distances (see Fig. 9d-f). Both 5-coordinate Fe1A and Fe2 local environments may be described as a "basally distorted square pyramid" [53]. Due to the contracted Fe1A-Ge2 distances, the Fe1A is nearer to the plane of the basal Ge2 atoms than Fe2 with the basal plane of the Ge3/4 atoms; however, Co1A/Co1B and Co2 have similar distances to the basal Ge plane. The structural differences of the Fe local environment compared to Co may contribute to the dissimilar magnetic properties. While neutron scattering experiments would be necessary to fully elucidate the role of Fe ordering in the magnetism of $Pr_4Fe_3Ge_{10}$ compared to the role of Co in $Pr_4Co_3Ge_{10}$, the difference in magnetism is likely not due to Pr-Pr interactions alone.

4. Conclusion

Crystals of the homologous series $Pr_{n+1}M_nGe_{3n+1}$ (M = transition metal), $Pr_4Fe_3Ge_{10}$ and $Pr_4Co_3Ge_{10}$, were grown using Sn flux. We characterized the disordered structure of $Pr_4Fe_3Ge_{10}$ with single crystal X-ray diffraction and compared the properties of the Fe and Co analogues of the homologous series. Additionally, we have shown that $Pr_4Fe_3Ge_{10}$ and $Pr_4Co_3Ge_{10}$ exhibit major differences in their magnetic properties including anisotropy, magnetic response, and the type of magnetic ordering. Further measurements, such as field dependent Mössbauer spectroscopy, neutron diffraction, or electron energy-loss spectroscopy may help elucidate the contribution of the lanthanide and transition metal sublattice to the magnetic properties. We illustrated the utility of using a homologous series as a platform to study collective phenomena in quantum materials with future work targeting the non-magnetic lanthanum analog to further our understanding of the role of the transition metal with respect to magnetism.

Associated content

CCDC 2272134 contains the supplementary crystallographic data for this paper. These data can be obtained free of charge via www.ccdc.cam.ac.uk/data_request/cif, or by emailing data_request@ccdc.cam.ac.uk, or by contacting The Cambridge Crystallographic Data Centre, 12 Union Road, Cambridge CB2 1EZ, UK; fax: +44 1223 336033.

CRediT authorship contribution statement

Melissa G. Anderson: Conceptualization, Data curation, Formal analysis, Investigation, Methodology, Visualization, Writing – original draft, Writing – review & editing. **Trent M. Kyrk**: Data curation, Visualization, Writing – review & editing. **Julia Chan**: Conceptualization, Funding acquisition, Investigation, Methodology, Project administration, Resources, Supervision, Writing – review & editing. **Gregory T. McCandless**: Methodology, Supervision, Writing – review & editing. **Ryan E. Baumbach**: Data curation, Resources. **Muhammad Zaeem Idrees**: Data curation, Formal analysis. **Sebastian A. Stoian**: Data curation, Formal analysis, Writing – original draft, Writing – review & editing.

Declaration of Competing Interest

The authors declare that they have no known competing financial interests or personal relationships that could have appeared to influence the work reported in this paper.

Data availability

Data will be made available on request.

Acknowledgments

Work at Baylor University was supported by the National Science Foundation (DMR-2209804), the Department of Energy (DE-SC0022068), and the Welch Foundation (AA-2056-20220101). Acknowledgment is made to the donors of the ACS Petroleum Research Fund for support of this research through a DNI grant to SAS. R.B. is supported by the National Science Foundation through DMR-1904361. The National High Magnetic Field Laboratory is supported by the National Science Foundation through NSFDMR-1644779 and the State of Florida. The authors acknowledge Alexis Dominguez Montero for his helpful discussions.

Appendix A. Supporting information

Supplementary data associated with this article can be found in the online version at doi:10.1016/j.jallcom.2023.172974.

References

[1] A. Weiland, J.B. Felder, G.T. McCandless, J.Y. Chan, One Ce, two Ce, three Ce, four? An intermetallic homologous series to explore: $A_{n+1}B_nX_{3n+1}$, Chem. Mater. 32 (2020) 1575–1580.
[2] W. Dörrscheidt, H. Schäfer, Die struktur des $BaPtSn_3$, $BaNiSn_3$ und $SrNiSn_3$ und ihre verwandtschaft zum $ThCr_2Si_2$-strukturtyp, J. Less-Common Met. 58 (1978) 209–216.
[3] O. Bodak, E. Gladyshevsky, Crystal structure of $CeNiSi_2$ and kindred compounds, Sov. Phys. Crystallogr. 14 (1970) 859–862.
[4] G. Brauer, A. Mittius, Die Kristallstruktur des Thoriumsilicids $ThSi_2$, Z. Anorg. Allg. Chem. 249 (1942) 325–339.
[5] P.A. Flinn, G.M. McManus, J.A. Rayne, Elastic constants of ordered and disordered Cu_3Au from 4.2 to 300°K, J. Phys. Chem. Solids 15 (1960) 189–195.
[6] M. Méot-Meyer, G. Venturini, B. Malaman, B. Roques, De Nouveaux Isotypes Lacunaires de $CeNiSi_2$: Les Germaniures RCo_xGe_2, R = Y, La-Sm, Gd-Lu, $0 < x \leqq 1$, Mater. Res. Bull. 20 (1985) 1515–1521.
[7] A. Weiland, K. Wei, G.T. McCandless, R.E. Baumbach, J.Y. Chan, Fantastic n = 4: $Ce_5Co_{4+x}Ge_{13-y}Sn_y$ of the $A_{n+1}M_nX_{3n+1}$ homologous series, J. Chem. Phys. 154 (2021), 114707.
[8] B. Belan, J. Stępeń-Damm, R. Gladyshevskii, O. Bodak, The new structure type $Ce_5Co_4Ge_{13}$, Chem. Met. Alloy. 1 (2008) 43–45.
[9] J.B. Felder, A. Weiland, H. Hodovanets, G.T. McCandless, T.G. Estrada, T.J. Martin, A.V. Walker, J. Paglione, J.Y. Chan, Law and disorder: special stacking units—building the intergrowth $Ce_6Co_5Ge_{16}$, Inorg. Chem. 58 (2019) 6037–6043.
[10] A. Weiland, K. Wei, G.T. McCandless, J.B. Felder, L.J. Eddy, R.E. Baumbach, J. Y. Chan, Strongly correlated electron behavior in a new member of the $A_{n+1}B_nX_{3n+1}$ homologous series: $Ce_7Co_6Ge_{19}$, Phys. Rev. Mater. 4 (2020), 074408.
[11] A. Thamizhavel, T. Takeuchi, T.D. Matsuda, Y. Haga, K. Sugiyama, R. Settai, Y. Ōnuki, Unique magnetic phases in an antiferromagnet $CeCoGe_3$, J. Phys. Soc. Jpn. 74 (2005) 1858–1864.
[12] V.K. Pecharsky, K.A. Gschneidner, $CeCo_{0.89}Ge_2$: a heavy-fermion system, Phys. Rev. B 43 (1991) 8238–8244.
[13] E.D. Mun, B.K. Lee, Y.S. Kwon, M.H. Jung, Kondo ground state of $CeCoGe_2$ with $j = 5/2$, Phys. Rev. B 69 (2004), 085113.
[14] J.G. Sereni, Evidence for valence fluctuation in the $CeSn_3$ compound, J. Phys. Met. Phys. 10 (1980) 2831.
[15] N.N. Efremova, Praseodymium valence state in $PrFe_{10}Mo_2PrNi_5$, and $PrNi_4M$ intermetallic compounds (M = Cu, Al, Ga), Phys. Solid State 47 (2005) 424.

[16] A. Yatskar, W.P. Beyermann, R. Movshovich, P.C. Canfield, Possible correlated-electron behavior from quadrupolar fluctuations in $PrInAg_2$, Phys. Rev. Lett. 77 (1996) 3637–3640.

[17] D. Destraz, L. Das, S.S. Tsirkin, Y. Xu, T. Neupert, J. Chang, A. Schilling, A. G. Grushin, J. Kohlbrecher, L. Keller, P. Puphal, E. Pomjakushina, J.S. White, Magnetism and anomalous transport in the Weyl semimetal PrAlGe: possible route to axial gauge fields, npj Quantum Mater. 5 (2020) 5.

[18] B. Meng, H. Wu, Y. Qiu, C. Wang, Y. Liu, Z. Xia, S. Yuan, H. Chang, Z. Tian, Large anomalous hall effect in ferromagnetic weyl semimetal candidate PrAlGe, APL Mater. 7 (2019), 051110.

[19] H.-Y. Yang, B. Singh, B. Lu, C.-Y. Huang, F. Bahrami, W.-C. Chiu, D. Graf, S.-M. Huang, B. Wang, H. Lin, D. Torchinsky, A. Bansil, F. Tafti, Transition from intrinsic to extrinsic anomalous Hall effect in the ferromagnetic weyl semimetal $PrAlGe_{1-x}Si_x$, APL Mater. 8 (2020), 011111.

[20] E.D. Bauer, N.A. Frederick, P.C. Ho, V.S. Zapf, M.B. Maple, Superconductivity and heavy fermion behavior in $PrOs_4Sb_{12}$, Phys. Rev. B 65 (2002), 100506.

[21] W. Higemoto, S.R. Saha, A. Koda, K. Ohishi, R. Kadono, Y. Aoki, H. Sugawara, H. Sato, Spin-triplet superconductivity in $PrOs_4Sb_{12}$ probed by Muon Knight Shift, Phys. Rev. B 75 (2007), 020510.

[22] M.A. Khan, G.T. McCandless, K.A. Benavides, T.J. Martin, A.M. Palacios, A.W. B. Samuel, D.P. Young, J.Y. Chan, Crystal growth and magnetic properties of $Pr_3Co_{2+x}Ge_7$ and the Sn-stabilized $Ln_3Co_{2+x}Ge_{7-y}Sn_y$ (Ln = Pr, Nd, Sm), Cryst. Growth Des. 18 (2018) 6028–6034.

[23] T.M. Kyrk, M. Bravo, G.T. McCandless, S.H. Lapidus, J.Y. Chan, Investigating the $A_{n+1}B_nX_{3n+1}$ homologous series: a new platform for studying magnetic praseodymium based intermetallics, ACS Omega 7 (2022) 19048–19057.

[24] Y. Lai, J.Y. Chan, R.E. Baumbach, Electronic landscape of the *f*-electron intermetallics with the $ThCr_2Si_2$ structure, Sci. Adv. 8 (2022), eabp8264.

[25] I. Das, E.V. Sampathkumaran, Magnetic behaviour of the interstitial alloys of the type, CeM_XGe_2 (M = Fe, Co, Ni and Cu), Solid State Commun. 83 (1992) 765–770.

[26] Z.P. Tener, V. Yannello, V.O. Garlea, S.H. Lapidus, P. Yox, K. Kovnir, S.A. Stoian, M. Shatruk, Evolution of bonding and magnetism via changes in valence electron count in $CuFe_{2-x}Co_xGe_2$, lnorg. Chem. 61 (2022) 4257–4269.

[27] H. Yamamoto, M. Ishikawa, K. Hasegawa, J. Sakurai, $CeFeGe_3$: a concentrated kondo compound with a stable valency and high Kondo temperature, Phys. Rev. B 52 (1995) 10136–10141.

[28] P. Skokowski, K. Synoradzki, M. Reiffers, A. Dzubinska, S. Rols, S. Arapan, D. Legut, T. Toliński, Effect of transition metals on the crystal field in $CeCo_{0.4}Fe_{0.6}Ge_3$, Intermetallics 153 (2023), 107776.

[29] P.C. Canfield, T. Kong, U.S. Kaluarachchi, N.H. Jo, Use of frit-disc crucibles for routine and exploratory solution growth of single crystalline samples, Philos. Mag. 96 (2016) 84–92.

[30] K. Yasukōchi, K. Kanematsu, T. Ohoyama, Magnetic properties of intermetallic compounds in iron-germanium system: $Fe_{1.67}Ge$ and $FeGe_2$, J. Phys. Soc. Jpn. 16 (1961) 429–433.

[31] A. Rossi, La Struttura, Cristallina delle Fasi $PrSn_3$ e $PrPb_3$, Gazz. Chim. Ital. 64 (1934) 832–834.

[32] L. Krause, R. Herbst-Irmer, G.M. Sheldrick, D. Stalke, Comparison of silver and molybdenum microfocus X-ray sources for single-crystal structure determination, J. Appl. Crystallogr. 48 (2015) 3–10.

[33] G.M. Sheldrick, SHELXT - integrated space-group and crystal-structure determination, Acta Crystallogr. A Found. Adv. 71 (2015) 3–8.

[34] G.M. Sheldrick, Crystal structure refinement with SHELXL, Acta Crystallogr. C Struct. Chem. 71 (2015) 3–8.

[35] J.Y. Ping, D.G. Rancourt, Absolute quantitative analysis by Mössbauer spectroscopy, Hyperfine Interact. 71 (1992) 1437–1440.

[36] J.Y. Ping, D.G. Rancourt, Failure of the direct HFD extraction method, Hyperfine Interact. 92 (1994) 1209–1212.

[37] T. Harmening, M. Eul, R. Pöttgen, Nickel-deficient stannides $Eu_2Ni_{2-x}Sn_5$–structure, magnetic properties, and Mössbauer spectroscopic characterization, Z. Naturforsch. B Chem. Sci. 64 (2009) 1107–1114.

[38] M. François, G. Venturini, B. Malaman, B. Roques, Nouveaux isotypes de $CeNiSi_2$≡ dans les Systemes R-M-X (R = La-Lu, M = Metaux des Groupes 7 A 11 ET X ≡ Ge, Sn). I Compositions et Parametres Cristallins, J. Less-Common Met. 160 (1990) 197–213.

[39] M.F. Fedyna, Isothermal sections of the praseodymium-iron-germanium system at 870 K, Neorg. Mater. 29 (1993) 63–65.

[40] H. Fukuoka, M. Yoshikawa, K. Baba, S. Yamanaka, Preparation and structures of lanthanoid germanides, $PrGe_{3.36}$, $NdGe_{3.25}$, and $TmGe_3$ with double square Ge-mesh structures, Bull. Chem. Soc. Jpn. 83 (2010) 323–327.

[41] O. Shcherban, I. Savysyuk, N. Semuso, R. Gladyshevskii, K. Cenzual, Crystal structure of the compound Pr_4Ge_7, Chem. Met. Alloy. (2009) 115–122.

[42] H. Yamamoto, M. Ishikawa, Low-temperature specific heat, magnetic susceptibility and electrical resistivity of $PrFeGe_3$, J. Phys. Soc. Jpn. 66 (1997) 965–966.

[43] R. Settai, K. Sugiyama, A. Yamaguchi, S. Araki, K. Miyake, T. Takeuchi, K. Kindo, Y. Ōnuki, Z. Kletowski, Magnetic and electrical properties in a dense kondo compound $PrSn_3$, J. Phys. Soc. Jpn. 69 (2000) 3983–3995.

[44] K.T. Matsumoto, N. Morioka, K. Hiraoka, Magnetic and thermodynamic properties of the Pr-based ferromagnet $PrGe_{2-\delta}$, Physica B 533 (2018) 90–92.

[45] T.M. Kyrk, E.R. Kennedy, J. Galeano-Cabral, K. Wei, G.T. McCandless, M.C. Scott, R.E. Baumbach, J.Y. Chan, Anisotropic magnetic and transport properties of orthorhombic *o*-$Pr_2Co_3Ge_5$, J. Phys. Mater. 5 (2022), 044007.

[46] T.M. Kyrk, J.P. Scheifers, K. Thanabalasingam, G.T. McCandless, D.P. Young, J. Y. Chan, It runs in the $BaAl_4$ family: relating the structure and properties of middle child $Ln_2Co_3Ge_5$ (Ln = Pr, Nd, and Sm) to its siblings $LnCo_2Ge_2$ and $LnCoGe_3$, lnorg. Chem. 60 (2021) 15343–15350.

[47] M.-A. Méasson, H. Muranaka, T. Kawai, Y. Ota, K. Sugiyama, M. Hagiwara, K. Kindo, T. Takeuchi, K. Shimizu, F. Honda, R. Settai, Y. Ōnuki, Magnetic properties of $RCoGe_3$ (R: Ce, Pr, and Nd) and strong anisotropy of the upper critical field in non-centrosymmetric compound $CeCoGe_3$, J. Phys. Soc. Jpn. 78 (2009), 124713.

[48] A. Szytuła, B. Penc, D. Kaczorowski, A. Arulraj, S. Baran, N. Stüsser, K. Tomala, Magnetic and electronic properties of RCo_xGe_2 (R=Pr, Nd) compounds, J. Alloy. Compd. 460 (2008) 120–124.

[49] P.B. Gütlich, E. Trautwein, Mössbauer Spectroscopy and Transition Metal Chemistry: Fundamentals and Application, Springer, Berlin, Heidelberg, 2011.

[50] P. Schobinger-Papamantellos, K.H.J. Buschow, Magnetic ordering of $TbNi_{0.4}Ge_2$ and $TbCu_{0.4}Ge_2$ studied by neutron diffraction and magnetic measurements, J. Alloy. Compd. 187 (1992) 73–80.

[51] W. Baželo, J. Leciejewicz, K. Maletka, A. Szytuła, Magnetic ordering in $TbNiGe_2$ and $HoNi_{0.64}Ge_2$ by neutron diffraction, J. Magn. Magn. Mater. 109 (1992) 305–308.

[52] P. Schobinger-Papamantellos, K.H.J. Buschow, C. Ritter, The (T, x) magnetic phase diagram of $TbNi_xGe_{-2}$ ($0.4 < x < 1$) compounds. A neutron study, J. Alloy. Compd. 287 (1999) 51–56.

[53] A.G. Blackman, E.B. Schenk, R.E. Jelley, E.H. Krenske, L.R. Gahan, Five-coordinate transition metal complexes and the value of τ_5: observations and caveats, Dalton Trans. 49 (2020) 14798–14806.